Progress In Electromagnetics Research C, Vol. 47, 95–101, 2014

Design and Characterization of a Dual-Band Metamaterial Absorber Based on Destructive Interferences

Saeid Jamilan[1, *], Mohammad N. Azarmanesh[1], and Davoud Zarifi[2]

Abstract—We present the design, characterization, and experimental verification of a dual-band metamaterial absorber (MA) in the microwave frequencies. The proposed MA consists of a metallic gammadion-shaped structure and a complete metal layer, separated by a dielectric spacer. The results show that the proposed MA has two absorption peaks at nearly 5.6 GHz and 6 GHz with absorption rates of 97% and 99%, respectively. The interference theory is used to investigate the physical mechanism of the proposed MA. The experimental results are in good agreement with the theoretical predictions. Furthermore, it is verified by simulations that the absorption of the proposed MA is almost insensitive to the incident wave polarization and oblique incident angle for the both *TM* and *TE* modes. This MA has broad prospect of potential applications.

1. INTRODUCTION

Metamaterial absorbers (MAs) have attracted considerable interests due to their unique properties such as high absorption and ultrathin thickness [1–3]. In recent years, the design of MAs with near-unity absorbance has been proposed at microwave and terahertz bands. These MAs have a number of potential applications such as radar-cross-section reduction, plasmonic sensors, selective thermal emitters, frequency selective bolometers, imaging, and solar cells [4–7].

In this paper, we present a planar MA which operates over microwave frequencies. It can absorb the EM wave at nearly 5.6 GHz and 6 GHz with absorption rates of 97% and 99%, respectively. The two absorptions are at C band. The physics of MAs has been explained by different mechanisms [8–11]. We use a numerical way to explore the absorption mechanism in this absorber structure and verify that the high absorption originates from the destructive interference of the reflection waves, but not the intrinsic electromagnetic resonance loss of the structure [12]. The full-wave simulations, numerical calculations, and experimental results support the proposed absorber's performance. Numerical simulations are performed using full-wave electromagnetic solver, CST Microwave Studio.

2. DESIGN AND THEORY

Our proposed MA consists of two conductive layers with a single dielectric spacer between them. The top layer has a gammadion-shaped structure and the bottom layer has a complete ground plate. The main goal of the complete ground plate on the bottom layer is zero transmission. The geometry of the proposed MA unit cell is described in Figures 1(a) and (b) with its design parameters and incident EM wave direction. The wave vector of the incident EM wave is perpendicular to the MA surface. The spacer of the absorber structure is the FR-4 ($\varepsilon_r = 4.3$ and $\tan\delta = 0.025$) with 1.5 mm thickness. Each of the metallic layers are made of copper with constant electric conductivity of 5.8×10^7 S/m and 0.02 mm thickness. In addition, the metallic ground plate is thicker than the penetration depth of the incident wave.

Received 13 December 2013, Accepted 29 January 2014, Scheduled 4 February 2014

* Corresponding author: Saeid Jamilan (saeid.jamilan@gmail.com).

[1] Department of Electrical Engineering, Urmia University, Urmia, Iran. [2] Antenna and Microwave Research Laboratory, School of Electrical Engineering, Iran University of Science and Technology, Tehran, Iran.

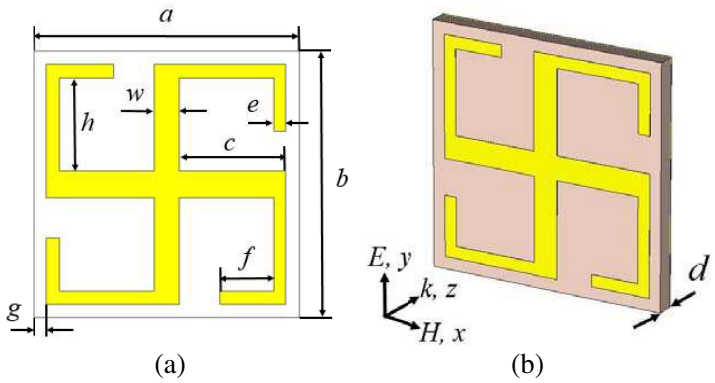

Figure 1. Unit cell geometry and design parameters. (a) Front view of the proposed MA unit cell with $a = b = 20\,\text{mm}$, $c = 8\,\text{mm}$, $e = 1\,\text{mm}$, $f = 4\,\text{mm}$, $h = 7\,\text{mm}$, $g = 1\,\text{mm}$, and $w = 2\,\text{mm}$. (b) Perspective view of the proposed MA unit cell with indicated incident EM wave direction and dielectric spacer thickness $d = 1.5\,\text{mm}$.

The full-wave simulations for one unit cell have done with CST Microwave Studio with periodic boundary condition (PBC) [13]. The boundary surfaces perpendicular to theincident E field are defined as perfect electric conductor (PEC) surfaces, while the surfaces perpendicular to the incident H field are defined as perfect magnetic conductor (PMC) surfaces. Lastly, the surfaces perpendicular to propagation vector (k) are defined as open ports. The simulation results of the reflection and absorption curve are shown in Figure 2. The absorption is calculated as $A = 1 - |S_{11}|^2 - |S_{21}|^2$, where $R = |S_{11}|^2$ is the reflection and $T = |S_{21}|^2$ is the transmission. The metal backing results in $|S_{21}| = 0$. From the results, we observe that near the frequencies of 5.6 GHz and 6 GHz the reflection coeffcient reaches to its minimum points and the absorption rate reaches to 97% and 99%, respectively.

To reveal the physical mechanism of the absorption, we use a model based on the destructive and constructive interferences at interfaces [14]. We model the gammadion-shaped structure as a metasurface with zero thickness to simplify the model. The metasurface acts as a part reflection surface (PRS) which can reflect/transmit part of the incident wave at the air-spacer interface. As shown in Figure 3, the model contains two interfaces: the air-spacer interface and ground plate.

At the air-spacer interface with gammadion-shaped structure, one part of the incident wave is reflected back to air with a reflection coefficient $R_{12} = r_{12}e^{i\alpha_{12}}$, and the other transmitted into the spacer with transmission coefficient $T_{12} = t_{12}e^{i\theta_{12}}$. The latter continues to propagate until it reaches the ground plate. After the reflection at the ground plane with reflection coefficient $r_{23} = -1$, partial reflection and transmission occur again at the air-spacer interface with coefficients $R_{21} = r_{21}e^{i\alpha_{21}}$ and

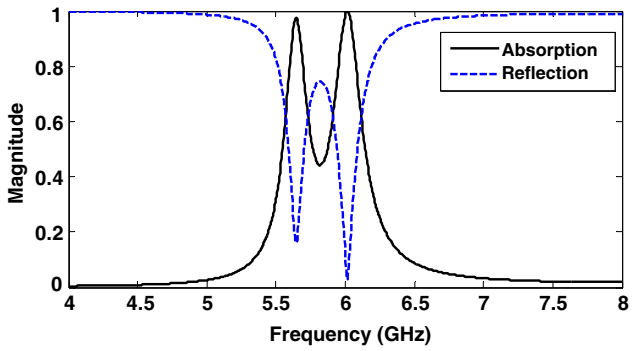

Figure 2. Simulated results of absorption (solid line) and reflection (dashed line).

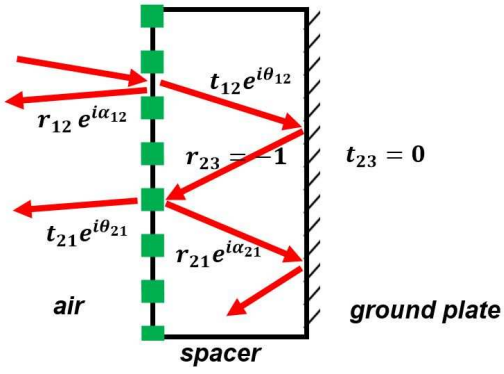

Figure 3. The model of interferences of the MA with the definition of the multiple reflection and transmission coefficients.

$T_{21} = t_{21}e^{i\theta_{21}}$. The multi-reflection process is illustrated in Figure 3. The overall reflection r is the sum of the direct reflection R_{12} and the multiple reflections at the air-spacer interface, as follows [15]:

$$\begin{aligned} r &= R_{12} + \frac{T_{12}T_{21}R_{23}e^{i2\beta}}{1 - R_{21}R_{23}e^{i2\beta}} = R_{12} - \frac{T_{12}T_{21}e^{i2\beta}}{1 + R_{21}e^{i2\beta}} \\ &= \frac{R_{12} + (R_{12}R_{21} - T_{12}T_{21})e^{i2\beta}}{1 + r_{21}e^{i(\alpha_{21}+2\beta)}} = \frac{R_{12} - (R_{12}R_{21} - T_{12}T_{21})e^{i(\pi+2\beta)}}{1 - r_{21}e^{i(\alpha_{21}+\pi+2\beta)}} \end{aligned} \tag{1}$$

where $\beta = -\frac{2\pi}{\lambda_0}nd$, λ_0 is the wavelength in free space, n is the refractive index of the dielectric spacer, and d is its thickness. To obtain the magnitude and phase coefficients of reflected and transmitted waves at the air-spacer interface, we run the CST Microwave Studio simulations based on the decoupled model of MA [12]. In this model, the ground plate of the unit cell is removed while the spacer and gammadion-shaped structure stay. Numerical simulations results of magnitude and phase coefficients of reflected and transmitted waves at the air-spacer interface are shown in Figures 4–7.

According to Equation (1), the near-unity absorption can be achieved when the reflection and transmission coefficients satisfy the following relations for the same frequency:

$$|R_{12}| - |R_{12}R_{21} - T_{12}T_{21}| \to 0 \tag{2}$$

$$\alpha_{21} + \pi + 2\beta \to 2m\pi, \quad m = 0, \pm1, \pm2, \ldots. \tag{3}$$

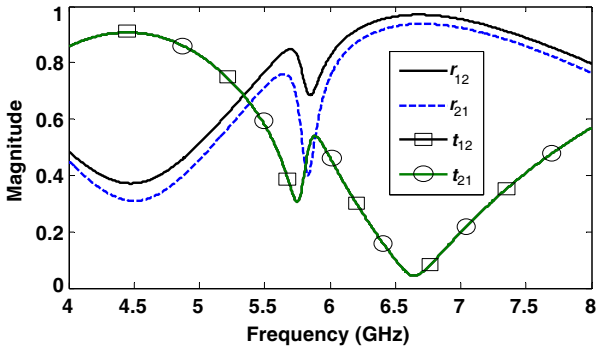

Figure 4. The simulated magnitudes of the reflection and transmission coefficients at the air-spacer interface based on the decoupled model of MA.

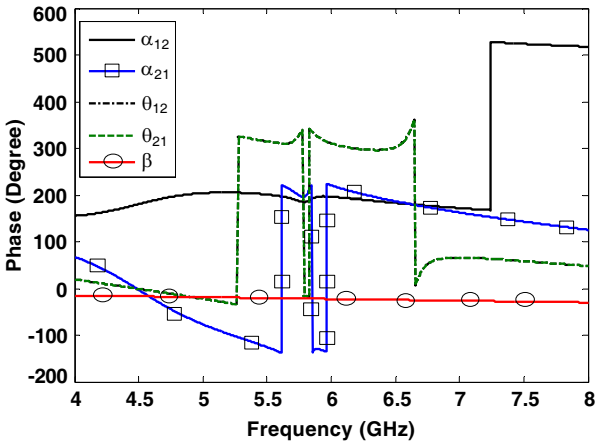

Figure 5. The simulated phases of the reflection and transmission coefficients at the air-spacer interface based on the decoupled model of MA.

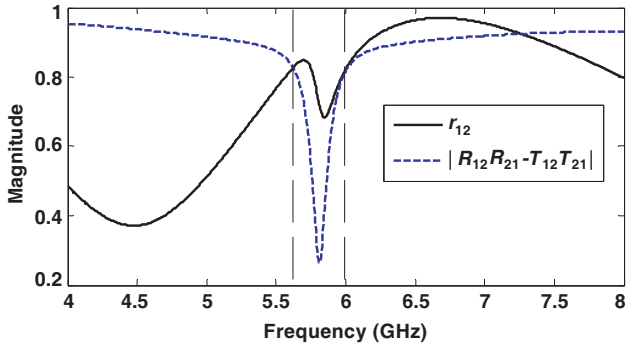

Figure 6. Calculated results of $|R_{12}| = r_{12}$ (solid line) and $|R_{12}R_{21} - T_{12}T_{21}|$ (dashed line).

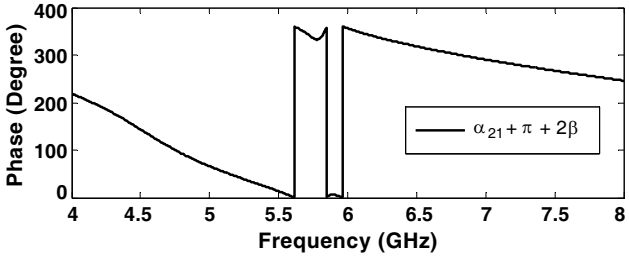

Figure 7. Calculated result of $\alpha_{21} + \pi + 2\beta$.

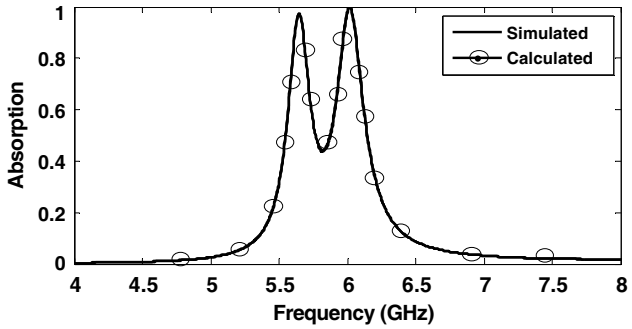

Figure 8. Simulated and calculated results of absorption.

As shown in Figures 6 and 7, the magnitudes of R_{12} (solid line) and $R_{12}R_{21} - T_{12}T_{12}$ (dashed line) cross each other at nearly absorption peak frequencies 5.6 GHz and 6 GHz and the phase condition of Equation (3) is also satisfied at nearly same frequencies. Thus, the magnitude and phase conditions are satisfied at absorption frequencies, resulting in the high absorption rate. As depicted in Figure 8, the calculated absorption curve using $A = 1 - |r|^2$ is in excellent agreement with the full-wave simulation result. This agreement validates the robustness of using interference theory to reveal the performance of proposed MA based on the destructive and constructive interferences at interfaces. This explanation does not involve any near-field interaction or magnetic resonance [8–11] between the two metal layers in the proposed MA.

3. FABRICATION AND EXPERIMENT

To verify the full-wave simulations and numerical calculations results, a 15×15 unit cells sample (300 mm $\times$ 300 mm $\times$ 1.5 mm) was fabricated by printing a planar array of designed gammadion-shaped structure on the front side and a complete ground plate on the back side of a FR-4 substrate (the thickness of the substrate is almost 1.5 mm) using printed-circuit-board (PCB) technology. The photograph of the experimental sample of proposed MA is shown in Figure 9. The schematic of reflection measurement is depicted in Figure 10. A vector network analyzer Agilent E8363C and two linear polarized horn antennas were used to transmit TEM waves in the range from 4 GHz to 8 GHz onto the sample and receive the reflected signals. The S_{21} output of the network analyzer, is related to the reflection from the surface of the MA. Since the location of the sample was far enough from the horn antennas, the incidence can be recognized as normal to the sample. As demonstrated in [16], the experimental measurement is carried out in two steps. In the first step, the reflection measurements should be calibrated using a sample-sized sheet of copper as a reflecting mirror. We measured a ground copper plane with the dimension the same as the sample and used the result as measurement reference.

Figure 9. Photograph of experimental sample of proposed MA.

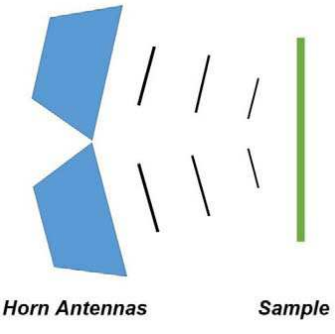

Figure 10. Schematic of reflection measurement. As shown, one of the horn antennas sends EM wave to the sample, while the other receives.

In the next step, we measured the fabricated sample of the metamaterial absorber and recorded the S_{21} parameters. The difference between the measured results of the first and second steps, represents the modified reflection coefficient from the proposed MA [16]. The modified measured reflection and simulated reflection as a function of the frequency are shown in Figure 11. It is observed that the numerical and experimental results are in a good agreement.

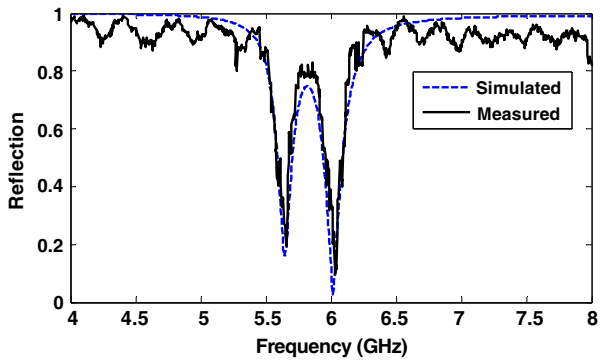

Figure 11. Measured (solid line) and simulated (dashed line) results of the reflection.

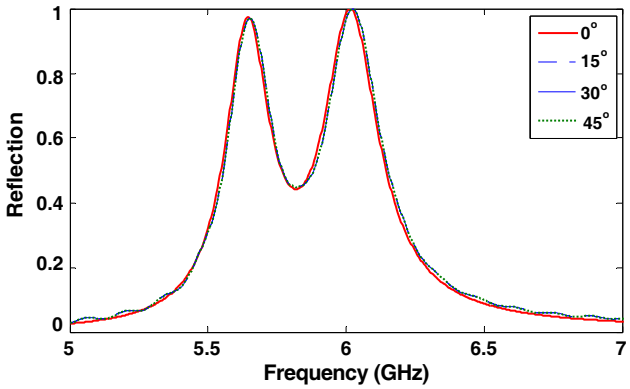

Figure 12. Simulated absorption curves for different polarizations at normal incidence.

4. POLARIZATION-INSENSITIVE AND WIDE-ANGLE ABSORPTION

To investigate the sensitivity of the proposed absorber to the polarization of the incident wave, we analyzed the absorptive characteristics under normal incident plane wave with different electric field polarizations. From the Figure 1, it is clear that the structure of proposed MA has a rotational symmetry about the wave vector (k). We change the polarization of the incident wave, by rotating the unit cell for different angles around the main radiation direction. Due to the symmetrical pattern of the proposed MA structure, angles from 0° to 45° are enough to verify the polarization insensitive absorber. The simulated results for different polarizations are shown in Figure 12. It can be observed from Figure 12 that the absorption curves remain almost unchanged. Thus, we can infer that the proposed MA is almost insensitive to the polarization of the incident wave.

In most of the practical applications, EM waves are usually incident onto absorbers with an oblique incident angle, so it is necessary to investigate the absorption under oblique incidence. The simulated absorption curve sat the different incident angles for both transverse magnetic (TM) and transverse electric (TE) polarized EM waves over a broad frequency range are plotted in Figures 13 and 14,

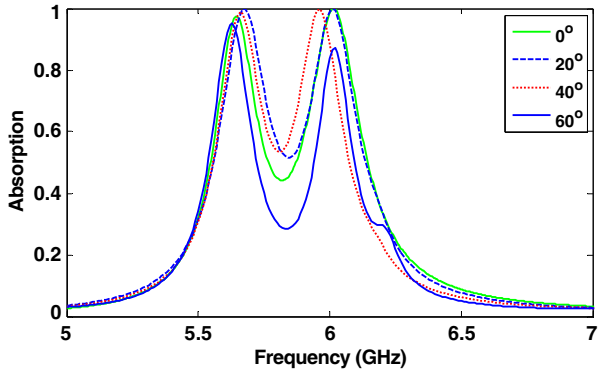

Figure 13. Simulated absorption curves at different oblique incident angles for TM mode.

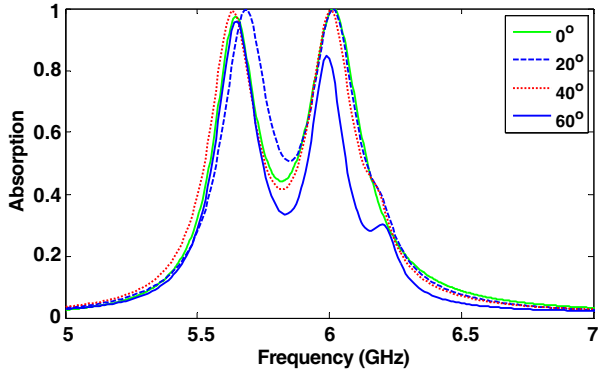

Figure 14. Simulated absorption curves at different oblique incident angles for TE mode.

respectively. The incident angles are made by deviating the wave vector (k) from the z-axis in yz-plane. It is observed from Figures 13 and 14 that the both of the absorptive peaks remain greater than 97% for the incident angles ranging from 0° to 40° for the both TM and TE waves. As the incident angles increase, the absorption rates decrease for both of the low and high frequency absorption bands. For an incident angle of 60°, the peak absorption drops to 95% (TM mode) and 96% (TE mode) at the low-frequency absorption band and 87% (TM mode) and 85% (TE mode) at the high-frequency absorption band. In addition, the changing of incident angle slightly shifts the frequencies of absorption bands for both TM and TE waves. These results indicate that the proposed MA is almost insensitive to the oblique incident EM waves over a large range of incident angles.

5. PARAMETRIC STUDY

The absorption frequencies can be altered by tuning the geometric features of the proposed MA, depending on the desired operation frequency spectrum. By altering w and f and fixing other parameters, the simulated results of absorption curves are shown in Figure 15. As w decreases from 2 mm to 1 mm, absorption frequencies at the low-frequency absorption band and high-frequency absorption band increase. With f increasing from 0 mm to 6 mm, as well as the value of w kept at 2 mm, the absorption frequencies decrease while the absorption rates change. As f increases, absorption rate at the high-frequency absorption band increases and low-frequency and high-frequency absorption bands get closer to each other.

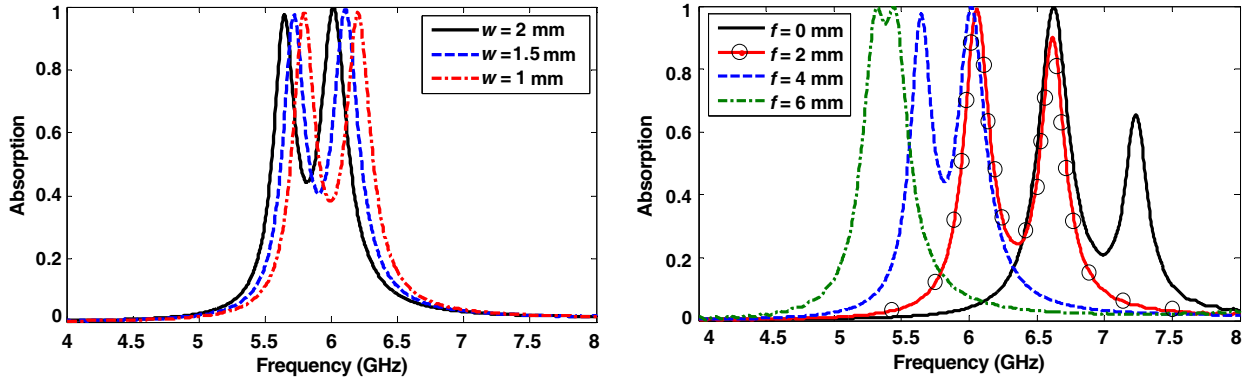

Figure 15. Effects of variation of different gammadion-shaped structure parameters on the performances of the proposed MA. (a) Variations of w. (b) Variations of f.

6. CONCLUSION

In this paper, we have demonstrated the design of a dual-band MA in the microwave regime. The proposed absorber structure showed 97% and 99% absorption at nearly 5.4 GHz and 6 GHz, respectively. The full-wave simulations, theoretical predictions based on the interference theory and experimental results were found to be in agreement with each other. It is the destructive interference between the direct reflection and the following multiple reflections that effectively traps incident wave in the proposed MA and causes the high absorption. With geometrical scalability, the proposed absorber could be designed to work at other frequency bands with nearly perfect absorption rates and this MA can has many potential application prospects, such as stealth technology, thermal detector, and imaging.

REFERENCES

1. Ye, Q., Y. Liu, H. Lin, M. Li, and H. Yang, "Multi-band metamaterial absorber made of multi-gap SRRs structure," *Appl. Phys. A*, Vol. 107, 155–160, 2012.

2. Huang, L. and H. Chen, "Multi-band and polarization insensitive metamaterial absorber," *Progress In Electromagnetic Research*, Vol. 113, 103–110, 2011.
3. Sun, L. K., H. F. Cheng, Y. J. Zhou, and J. Wang, "Low-frequency and broad band metamaterial absorber: design, fabrication, and characterization," *Appl. Phys. A*, Vol. 105, 49–53, 2011.
4. Diem, M., T. Koschny, and C. M. Soukoulis, "Wide-angle perfect absorber/thermal emitter in the terahertz regime," *Phys. Rev. B*, Vol. 79, No. 3, 033101, 2009.
5. Landy, N., C. Bingham, T. Tyler, D. Smith, and W. Padilla, "Design, theory, and measurement of a polarization-insensitive absorber for terahertz imaging," *Phys. Rev. B*, Vol. 79, No. 12, 125104, 2009.
6. Liu, N., M. Mesch, T. Weiss, M. Hentschel, and H. Giassen, "Infrared perfect absorber and its application as plasmonic sensor," *Nano Lett.*, Vol. 10, No. 7, 2342–2348, 2010.
7. Noor, A. and Z. Hu, "Metamaterial dual polarised resistive Hilbert curve array radar absorber," *IET Microw. Antennas Propag.*, Vol. 4, 667–673, 2010.
8. Landy, N. I., S. Sajuyigbe, J. J. Mock, D. R. Smith, and W. J. Padilla, "Perfect metamaterial absorber," *Phys. Rev. Lett.*, Vol. 100, 207402, 2008.
9. Lee, H.-M. and H.-S. Lee, "A dualbandmetamaterial absorber based with resonant-magnetic structures," *Progress In Electromagnetic Research*, Vol. 33, 1–12, 2012.
10. Xu, Y. Q., P. H. Zhou, H. B. Zhang, L. Chen, and L. J. Deng, "A wide-angle planar metamaterial absorber based on split ring resonator coupling," *J. Appl. Phys.*, Vol. 110, 044102, 2011.
11. Dincer, F., M. Karaaslan, E. Unal, and C. Sabah, "Dual-band polarization independent metamaterial absorber based on omega resonator and octa-starstrip configuration," *Progress In Electromagnetic Research*, Vol. 141, 219–231, 2013.
12. Chen, H.-T., "Interference theory of metamaterial perfect absorbers," *Opt. Express*, Vol. 20, No. 7, 7165–7172, 2012.
13. Okano, Y., S. Ogino, and K. Ishikawa, "Development of optically transparent ultrathin microwave absorber for ultrahigh-frequency RF identification system," *IEEE Trans. Microw. Theory Tech.*, Vol. 60, 2456–2464, 2012.
14. Chen, H.-T., J. Zhou, J. F. O'Hara, F. Chen, A. K. Azad, and A. J. Taylor, "Antireflection coating using metamaterials and identification of its mechanism," *Phys. Rev. Lett.*, Vol. 105, 073901, 2010.
15. Alaee, R., M. Farhat, C. Rockstuhl, and F. Lederer, "A perfect absorber made of graphene micro-ribbon metamaterial," *Opt. Express*, Vol. 20, No. 27, 2012.
16. Abdalla, M. A., "Experimental verification of a triple band thin radar absorber metamaterial for oblique incidence applications," *Progress In Electromagnetic Research*, Vol. 39, 63–72, 2013.